Nanoscale Advances

ROYAL SOCIETY OF CHEMISTRY

PAPER

View Article Online
View Journal | View Issue

Cite this: *Nanoscale Adv.*, 2024, **6**, 481

In situ growth of copper oxide on MXene by combustion method for electrochemical ammonia production from nitrate†

Sagar Ingavale,[a] Phiralang Marbaniang,[b] Manoj Palabathuni[a] and Nimai Mishra *[c]

The elimination of the nitrogen pollutant nitrate ions through the electrochemical synthesis of ammonia is an important and environment friendly strategy. Electrochemical nitrate reduction requires highly efficient, selective, and stable catalysts to convert nitrate to ammonia. In this work, a composite of copper oxide and MXene was synthesized using a combustion technique. As reported, nitrate ions are effectively adsorbed by Cu_xO (CuO & Cu_2O) nanoparticles. Herein, MXene is an excellent assembly for anchoring Cu_xO on its layered surface because it has a strong support structure. Powder X-ray diffraction (XRD), X-ray photoelectron spectroscopy (XPS), scanning electron microscopy (SEM), and transmission electron microscopy (TEM) analyses show the presence of oxidation states of metal ions and the formation of Cu_xO nanofoam anchors on the surface of MXene ($Ti_3C_2T_x$). The optimized $Cu_xO/Ti_3C_2T_x$ composite exhibits an improved nitrate reduction reaction. The electrochemical studies of $Cu_xO/Ti_3C_2T_x$ show an interesting nitrate reduction reaction (NO_3RR) with a current density of 162 mA cm^{-2}. Further, $Cu_xO/Ti_3C_2T_x$ shows an electrocatalytic activity with an ammonia production of 41 982 μg h^{-1} m_{cat}^{-1} and its faradaic efficiency is 48% at −0.7 V *vs.* RHE. Thus, such performance by $Cu_xO/Ti_3C_2T_x$ indicates a well-suitable candidate for nitrate ion conversion to ammonia.

Received 7th August 2023
Accepted 23rd November 2023

DOI: 10.1039/d3na00609c

rsc.li/nanoscale-advances

1. Introduction

Ammonia is a basic nitrogen source for industrial applications widely used for manufacturing fertilizers, pharmaceuticals, textiles, and plastics.[1,2] Ammonia is mostly synthesized by the traditional Haber–Bosch process, requiring high temperature and pressure to convert nitrogen and hydrogen gases to ammonia in the presence of a iron-based catalyst.[3] Though the preparation of ammonia is carbon-free, it consumes >1% of the global energy supply (the energy obtained by burning huge amounts of fossil fuels resulting in hundreds of millions of tons of CO_2 release).[4] The electrochemical conversion of nitrogen to ammonia at ambient conditions is the best approach as an alternative and environmentally friendly method.[5] However, the direct electrochemical reduction of N_2 to ammonia is hindered due to the high energy barrier necessary for breaking the inert N≡N bond, the poor contact between non-polar N_2 and active sites of catalysts, and the low solubility of N_2 in water.[6–8] In contrast, nitrates have special benefits as nitrogen sources for the electro-synthesis of NH_3, as the polar N–O bond has a bond energy that is four times lower than the non-polar N≡N triple bond (204 kJ mol^{-1}), allowing the N–O bond to be easily activated at lower energies.[9] Nitrate is widely distributed in the environment and builds up over time as a result of industrial

[a]*Department of Chemistry, SRM University-AP, Andhra Pradesh, Neerukonda, Guntur (Dt), Andhra Pradesh, 522240, India*

[b]*Department of Chemistry, Indian Institute of Technology Madras, Chennai 600036, India*

[c]*Institute of Chemical Technology Mumbai, IOC Odisha Campus Bhubaneswar, Bhubaneswar, Odisha, 751013, India. E-mail: n.mishra@iocb.ictmumbai.edu.in*

† Electronic supplementary information (ESI) available: The details of materials used for the synthesis of $Cu_xO/Ti_3C_2T_x$, physical characterization, electrochemical measurements and determination of the concentration of ammonia (including the faradaic efficiency and NH_3 yield) are given. XPS survey spectra for Cu_xO and $Cu_xO/Ti_3C_2T_x$. LSVs curve for Cu_xO-2/$Ti_3C_2T_x$, $Cu_xO/Ti_3C_2T_x$ and Cu_xO-3/$Ti_3C_2T_x$ at 10 mV s^{-1} with nitrate ions in 0.1 M K_2SO_4 electrolyte. Comparative LSV pattern at 10 mV s^{-1} and chronoamperometric curve of Cu_xO, $Ti_3C_2T_x$, and $Cu_xO/Ti_3C_2T_x$ with nitrate ions in 0.1 M K_2SO_4 electrolyte. NH_3 yield and faradaic efficiency for NH_3 production of Cu_xO, $Ti_3C_2T_x$, and $Cu_xO/Ti_3C_2T_x$ catalysts at −0.7 V *vs.* RHE. UV-Vis spectra for indo-phenol determination of different known concentrations of NH_4^+ standards. Calibration curve obtained from linear fit. Photograph of standard NH_4^+ solution. UV-Vis spectra for Watt and Chrisp determination of different known concentrations of hydrazine standards. Calibration curve obtained from linear fit. Photograph of standard hydrazine solution. Electrocatalytic *i–t* experiments at various applied potentials of $Cu_xO/Ti_3C_2T_x$ catalyst, UV-Vis spectra for indo-phenol determination of ammonia and Watt and Chrisp determination of hydrazine in electrolytes obtained from electrocatalytic CA experiments at different applied potentials respectively. Photograph of ammonia and hydrazine solution. UV-Vis spectra for Watt and Chrisp determination of hydrazine in electrolytes obtained from electrocatalytic CA experiments at −0.7 V *vs.* RHE. Chronoamperometric analysis of $Cu_xO/Ti_3C_2T_x$ catalyst at −0.7 V *vs.* RHE in 0.5 M KNO_3 + 0.1 M K_2SO_4 electrolyte. Comparative current *vs.* scan rate profile; (b) ECSA and roughness factor for Cu_xO, $Ti_3C_2T_x$, and $Cu_xO/Ti_3C_2T_x$ electrocatalysts. See DOI: https://doi.org/10.1039/d3na00609c

and agricultural production activities, mostly having negative impacts on aquatic ecosystems and human health, including methemoglobinemia development, thyroid effects, and cancer.[10–12] Hence, the electroreduction of nitrate for NH_3 generation not only complies with energy sustainability but also serves as a strategy to reduce pollution.

The adsorption of nitrate ions, deoxygenation of the N-species, hydrogenation of the N-species, and desorption of the reduced species are the steps involved during the conversion of NO_3^- ions to NH_3 on the electrode surface by the electroreduction process.[13] A copper (Cu)-based catalyst was recently developed for nitrate reduction with >90% faradaic efficiency (FE).[14] Cu-based composites with different particle sizes and oxidation states were studied and observed to have multiple active sites for ammonia production from nitrate ions.[15] Generally, copper easily gets oxidized. The effect of the oxidation state of Cu on the activity and selectivity of NO_3 electroreduction to NH_3 is still unknown.[15] According to Zhao *et al.*, a Cu_2O film formed on Cu foam exhibits catalytic activity for NO_3RR. It is stated that the creation of a strong preferred (111) orientation and a nanopyramid terminated on the surface of the Cu_2O film account for the increased efficiency and selectivity for ammonia production.[16] Gong *et al.* reported that Cu_2O, subjected to plasma treatment, provides a hydroxyl group-rich surface and a high concentration of oxygen vacancies, resulting in greater charge density near the Cu sites and an upshifted d-orbital.[17] The treated Cu_2O enhances electron transport between the surface and chemical intermediates, making NO_3RR more favourable. Furthermore, to enhance electron transport, Zhang *et al.* generated electron-deficient Cu by dispersing Au particles on the surface of Cu (111), allowing electrons to move from Cu to Au atoms.[1] Similarly, CuPd nanocubes favour NO_3^- ion adsorption because the Cu sites favour bridge-bidentate NO_3^- adsorption and increase ammonia production due to Pauli repulsion between *N and the d-orbital of Pd, which facilitates protonation of N-bonded species towards NH_3.[18] Cu nanowires supported by Ru (Ru–CuNW) also improve the adsorption of NO_3^- ions, allowing it to hydrogenate with N atoms better than CuNW.[13] However, it is not preferred to use expensive metals, and Wang's group claims that oxidised Cu metal, *i.e.*, CuO exhibits strong adsorption towards NO_3^- ion.[19] Additionally, MXene ($Ti_3C_2T_x$: T_x = Cl^-, OH^- and F^-) possesses excellent conductivity, hydrophilicity, large specific surface area, and exceptionally rich surface groups thanks to its distinctive structural characteristics. Because of its huge surface area and high concentration of surface groups, it serves as an excellent anchoring and dispersal medium for a wide variety of electrocatalysts.[20,21]

An interesting electrocatalytic activity towards NO_3RR can be expected from a composite of Cu_xO and MXene due to Cu_xO potency at adsorbing nitrate ions and MXene potency at supporting Cu_xO on its surface. Therefore, in this study, we developed an efficient electrocatalyst for NH_3 generation by *in situ* growing Cu_xO on MXene *via* a combustion approach. The presence of metal ion oxidation states and the creation of a Cu_xO nanofoam anchor on the surface of $Ti_3C_2T_x$ are evidenced by powdered-XRD, XPS, SEM, and TEM analyses. The electrochemical reduction of nitrate by $Cu_xO/Ti_3C_2T_x$ was demonstrated in the presence and absence of nitrate ions. The electrochemical studies of $Cu_xO/Ti_3C_2T_x$ show interesting NO_3RR with a current density of 162 mA cm^{-2}. Further, $Cu_xO/Ti_3C_2T_x$ shows an electrocatalytic activity with ammonia production of 41 982 μg h^{-1} m_{cat}^{-1} and its faradaic efficiency is 48% at −0.7 V *vs.* RHE. Thus, such performance by $Cu_xO/Ti_3C_2T_x$ indicates a well-suitable candidate for nitrate ion conversion to ammonia. In the future, similar composites with various synthesis techniques may be highlighted for NO_3 reduction to ammonia.

2. Experimental section

2.1. Chemicals and materials

All chemicals purchased were of analytical grade (refer ESI†) and used without being tested for purity.

2.2. Synthesis of MXene ($Ti_3C_2T_x$) from MAX phase (Ti_3AlC_2)

MXene ($Ti_3C_2T_x$) was synthesized from the MAX phase (Ti_3AlC_2) using the methods described in the recently published article. In brief, 500 mg of Ti_3AlC_2 powder was sonicated and stirred at room temperature for 24 hours in HF (40 wt%) solution. The solution was centrifuged at 5000 rpm and was rinsed in deionized water until the pH was neutral, resulting in nanosheets of $Ti_3C_2T_x$.

2.3. Preparation of copper oxide and MXene composite

Copper oxide and MXene composites were synthesized using a simple combustion process. 500 mg of $Cu(NO_3)_2 \cdot 6H_2O$ and 20 mg of MXene were mixed together in 1 ml of ethylene glycol for 15 minutes until a homogeneous dispersed solution was achieved. A Petri dish was pre-heated for 15 minutes at 250 °C. The solution is then poured into a Petri dish, where an immediate combustion reaction occurs with the effervescence to generate copper oxide and MXene composite. The product was collected and labelled as $Cu_xO/Ti_3C_2T_x$ after cooling to ambient temperature. Similarly, composites were optimized using the same technique and by altering the weight ratio of $Cu(NO_3)_2 \cdot 6H_2O$ by 250 mg and 750 mg, respectively, and are indicated as Cu_xO-1/$Ti_3C_2T_x$ and Cu_xO-2/$Ti_3C_2T_x$. Similar steps were taken to synthesise Cu_xO, but in the absence of $Ti_3C_2T_x$.

3. Results and discussion

MXene ($Ti_3C_2T_x$) was synthesized from the MAX phase (Ti_3AlC_2) by etching Al in a 40% HF solution. The as-prepared $Ti_3C_2T_x$ was first homogeneously dispersed in ethylene glycol with $Cu(NO_3)_2 \cdot 6H_2O$, followed by a combustion technique in order to self-assemble Cu_xO on $Ti_3C_2T_x$. MXene is a well-known material in the current research due to its excellent properties especially electrical conductivity, which is the highest among all synthesized 2D materials, more than ten times the conductivity of reduced graphene oxide (rGO) films. It is also a good supporter because of the consistent negative charge at the surface of $Ti_3C_2T_x$, which attracts the positively charged ions

like Cu^{2+} and Cu^{+} on its surface. Fig. 1 depicts a schematic illustration of the $Cu_xO/Ti_3C_2T_x$ synthesis.

The crystal structures of $Cu_xO/Ti_3C_2T_x$ composites were compared to those of $Ti_3C_2T_x$ and Cu_xO using XRD analysis, as shown in Fig. 2(a). The presence of a peak at 8.4° suggests the production of exfoliated layers corresponding to the (002) plane.[22] The peak at 8.4° moved to a broad peak at 11.6° along with the appearance of other Cu_xO peaks after Cu_xO self-assembled on $Ti_3C_2T_x$, confirming the composite creation of Cu_xO and $Ti_3C_2T_x$. $Cu_xO/Ti_3C_2T_x$ composites show diffraction peaks for CuO at 32.5°, 35.5°, 38.6°, 48.7°, 53.6°, 58.1°, 61.5°, 66.2°, 68.0° and 73.7°, corresponding to Miller indices (110), (002), (111), (−202), (020), (202), (−113), (−311), (220), and (221), respectively (agreed with reference code JCPDS no. 01-089-5898). It is also observed that the peaks of Cu_2O at 29.5° 36.4°, 42.3°, and 61.5° correspond to (110), (111), (200), and (220) planes, respectively (JCPDS no. 01-078-2076). Thus, from XRD analysis, it is observed that Cu_xO in the composite retains the same crystal structure as compared to the as-prepared Cu_xO. The comparative survey spectra of Cu_xO and $Cu_xO/Ti_3C_2T_x$ are given in Fig. S1† to provide the relative abundance of elements. Both the catalysts display the presence of Cu 2p metal. XPS analysis was used to determine the chemical state of $Cu_xO/Ti_3C_2T_x$, and Gaussian fitting was used to deconvolute the C 1s, Ti 2p, Cu 2p, and O 1s core levels. Fig. 2(b) depicts the deconvoluted C 1s core level as four peaks at 283.6 eV, 284.7 eV, 285.9 eV, and 288.7 eV, which correspond to the C–Ti, C=C, C–O, and C=O bonds, respectively.[22] The deconvoluted peaks of Cu(II) and Cu(I) states are shown in Fig. 2(c). Peaks at 934.9 eV and 954.1 eV are assigned to Cu $2p_{3/2}$ and Cu $2p_{1/2}$, respectively, and the gap between these peaks is 19.2 eV, which coincides well with the creation of CuO on the composite.[23] The peaks at 933.6 eV and 953.6 eV are attributed to Cu $2p_{3/2}$ and Cu $2p_{1/2}$, respectively, which represented Cu_2O. The main Cu $2p_{3/2}$ peak at 934.9 eV is accompanied by two satellite peaks on the higher binding energy side at around 944.3 eV and 941.8 eV, indicating the presence of CuO.[24,25] Fig. 2(c) clearly depicts the main peak of Cu $2p_{1/2}$ at 954.1 eV and its satellite peak at 962.5 eV, which also confirms the presence of CuO. Because of the presence of the partially filled d^9 shell arrangement in the ground state, the CuO (Cu(II)) spectrum shows prominent shake-up satellite features, whereas no shake-up satellite is seen for Cu_2O (Cu(I)) due to its filled d^{10} arrangement in the ground state. Fig. 2(d) depicts the core level of Ti 2p deconvoluted into two peaks at 458.3 eV and 464.4 eV, which correspond to the Ti–C and Ti–O bonds, respectively.[22] The appearance of Ti–O bonding could be due to oxidation during the combustion process, which converts unstable Ti–C bonds to Ti–O bonds. Furthermore, as seen in Fig. 2(e), the O 1s core level is deconvoluted into two peaks, 530.0 eV and 532.2 eV, which correspond to the metallic oxygen and O=C bonds, respectively.

Surface morphologies and microstructures of $Ti_3C_2T_x$ and $Cu_xO/Ti_3C_2T_x$ samples were examined using SEM and TEM, respectively. Fig. 3(a) displays a typical $Ti_3C_2T_x$ nanosheet layered structure with an accordion-like structure, and the separated layer of $Ti_3C_2T_x$ nanosheets suggests successful aluminium etching from the MAX phase. The TEM image of $Ti_3C_2T_x$ revealed exfoliated nanoflakes with distinct edges (Fig. 3(b)), and crystallinity was confirmed by the HRTEM image with interplanar spacing of 0.19 nm (Fig. 3(c)). The nanoflakes distinct edges of $Ti_3C_2T_x$ may be required for *in situ* Cu_xO development on its surfaces, which may promote nitrate ion adsorption, charge transfer, and electron transport. Fig. 3(d) indicates that Cu_xO is evenly distributed on $Ti_3C_2T_x$, owing to the combustion process, which produces a smooth nanofoam of Cu_xO on the surface of MXene (a Cu_xO nanofoam structure is created as a result of nitrate ions escaping from the precursor during the combustion process). As shown in Fig. 3(f), the interplanar spacing values were 0.25 nm, which is in good agreement with the (111) plane of Cu_2O. Consequently, the formation of $Cu_xO/Ti_3C_2T_x$ is evident from the morphologies.

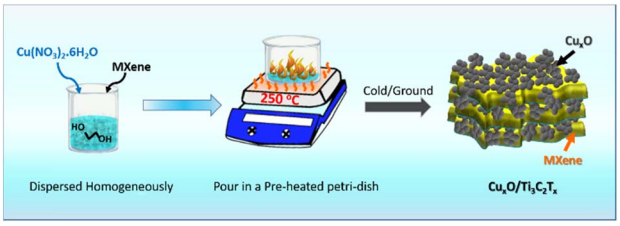

Fig. 1 Schematic illustration of the preparation of the $Cu_xO/Ti_3C_2T_x$ composite.

4. Electrochemical nitrate reduction by $Cu_xO/Ti_3C_2T_x$ catalysts

Electrochemical ammonia production is an environment friendly process because it converts nitrate waste into a valuable ammonia product. Consequently, electrochemical measurements were conducted on the $Cu_xO/Ti_3C_2T_x$ composite, and the construction of electrodes is described in ESI.† Initially, we employed 0.1 M K_2SO_4 solution with and without nitrate ions (0.5 M KNO_3) to conduct the electrochemical nitrate reduction to ammonia using the linear sweep voltammetry (LSV) technique. As shown in Fig. 4(a), the LSVs show that nitrate reduction occurs when compared to the competent hydrogen evolution reaction. The neutral electrolyte, 0.1 M K_2SO_4, aids in minimizing the HER reaction and improving nitrate reduction. The current density was determined to be around 162 mA cm^{-2} in the presence of nitrate solution and around 43 mA cm^{-2} in the absence of nitrate solution, demonstrating a successful electrochemical nitrate reduction reaction. After adding nitrate solution, the overpotential was reduced to approximately 310 mV to obtain a current density of 20 mA cm^{-2}. Along with the optimized composite, the nitrate reduction of other controlled catalysts was analysed using LSV and shown in Fig. S2.† The significance of synergetic effects between Cu_xO and $Ti_3C_2T_x$ composite was assessed by comparing the NO_3RR catalytic activity of Cu_xO, $Ti_3C_2T_x$, and the optimised $Cu_xO/Ti_3C_2T_x$ composite, as shown in Fig. S3.† At −0.7 V *vs.* RHE, the current density for Cu_xO, $Ti_3C_2T_x$, and $Cu_xO/Ti_3C_2T_x$ is determined to be roughly 45 mA cm^{-2}, 37 mA cm^{-2}, and 162 mA

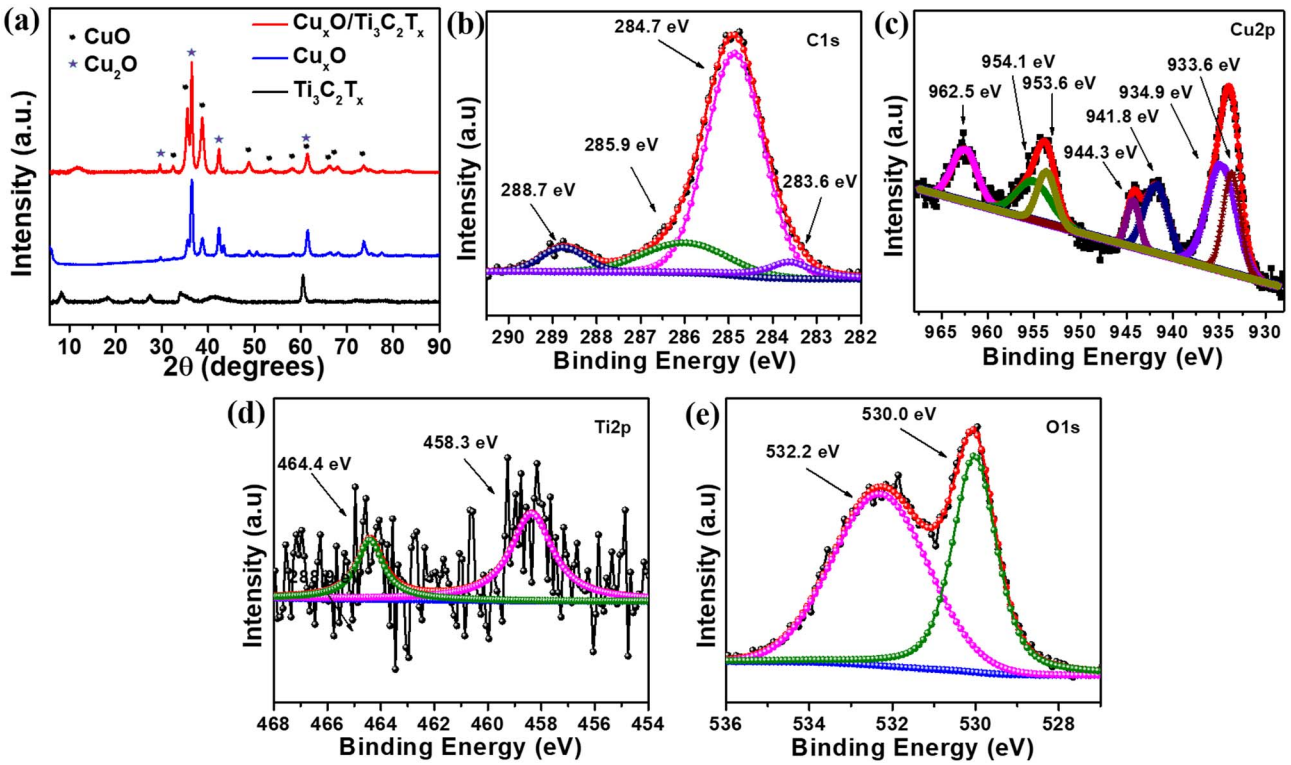

Fig. 2 (a) Comparative XRD patterns of $Ti_3C_2T_x$, Cu_xO and $Cu_xO/Ti_3C_2T_x$. Deconvoluted XPS spectrum for (b) C 1s, (c) Cu 2p, (d) Ti 2p and (e) O 1s of $Cu_xO/Ti_3C_2T_x$ composite.

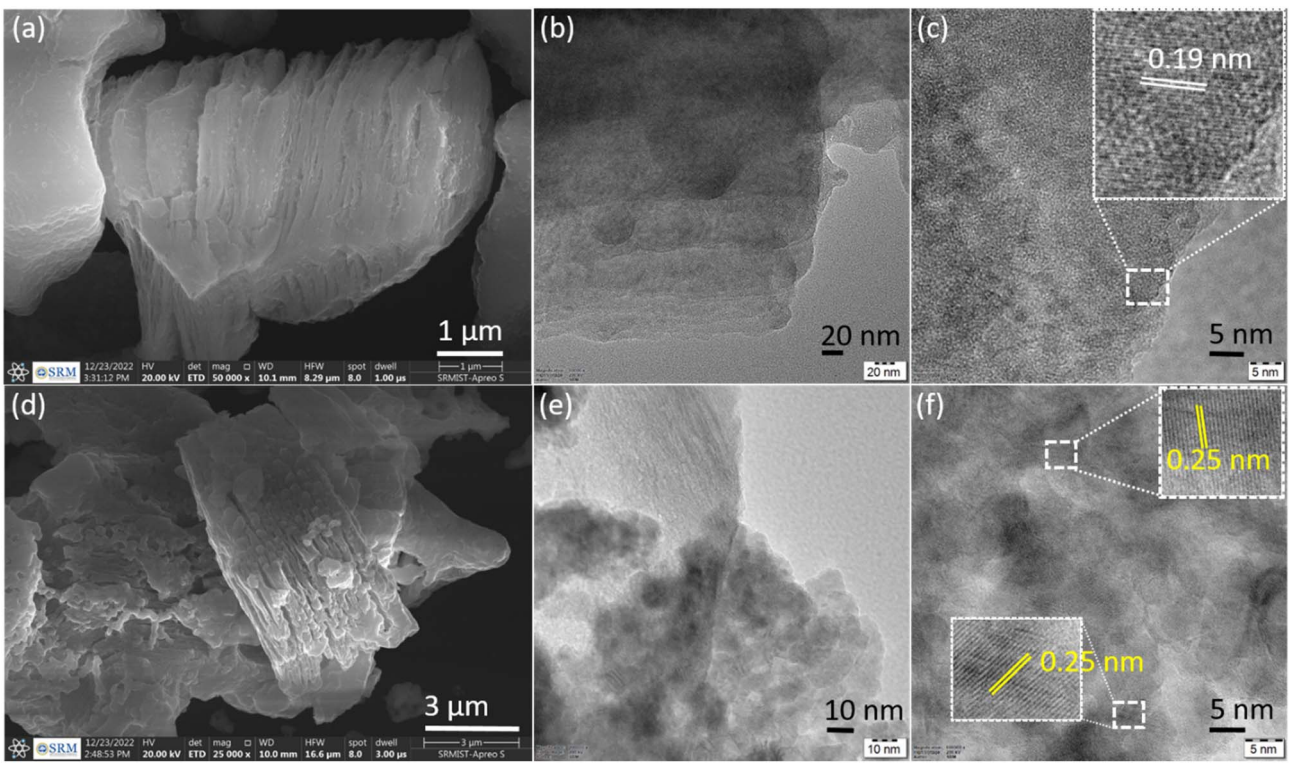

Fig. 3 SEM of (a) $Ti_3C_2T_x$ and (d) $Cu_xO/Ti_3C_2T_x$ composite. TEM image of (b and c) $Ti_3C_2T_x$ and (e and f) $Cu_xO/Ti_3C_2T_x$ composite.

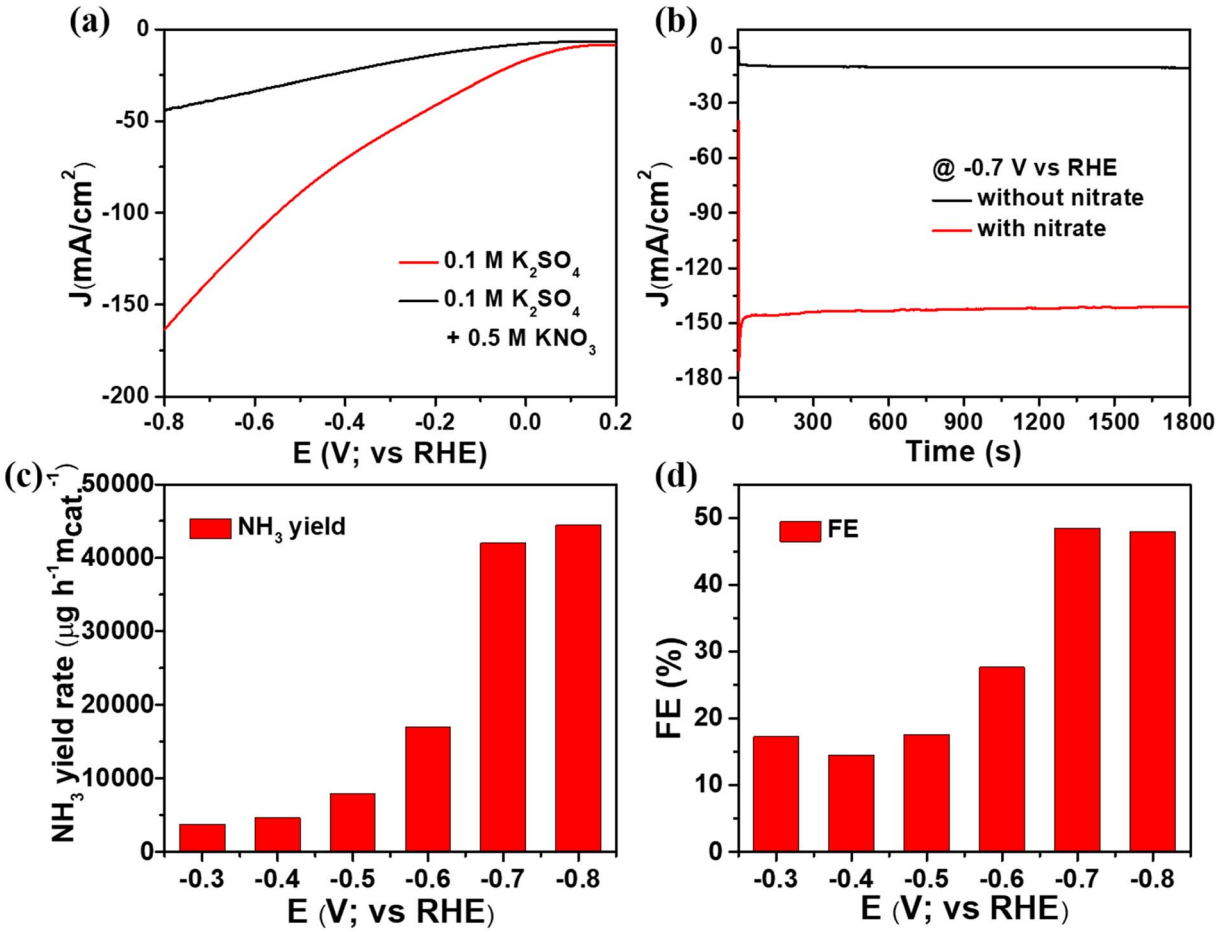

Fig. 4 (a) LSVs curve for $Cu_xO/Ti_3C_2T_x$ at 10 mV s^{-1} with and without nitrate ions in 0.1 M K_2SO_4 electrolyte, (b) chronoamperometric measurements at −0.7 V *vs.* RHE with and without nitrate ions (c) NH_3 yield and (d) faradaic efficiency for NH_3 production of $Cu_xO/Ti_3C_2T_x$ catalyst at various potentials.

cm^{-2}, respectively (Fig. S3(a)†). According to a chronoamperometry investigation, the current density for Cu_xO, $Ti_3C_2T_x$, and $Cu_xO/Ti_3C_2T_x$ was found to be approximately 28 mA cm^{-2}, 32 mA cm^{-2}, and 150 mA cm^{-2}, respectively, at −0.7 V, as shown in Fig. S3(b).† It is obvious that the composite catalyst outperforms the Cu_xO or $Ti_3C_2T_x$ catalysts by three times due to their synergy effect. This is because $Ti_3C_2T_x$ solely (consisting of a negatively charged surface) is unfavourable to adsorb the electron-rich nitrate due to electrostatic repulsion. Whereas, Cu_xO is favourable but the poor conductivity properties decrease the electroreduction of nitrate ions. As a result, as compared to either Cu_xO or $Ti_3C_2T_x$ alone, the combination of $Ti_3C_2T_x$ and Cu_xO provides an excellent activity for the nitrate reduction reaction. Consequently, the NH_3 yield and FE of the optimized composite were determined using the chronoamperometric method, which consisted of conducting experiments at varying potentials with time. The electrolyte was collected after 30 minutes of analysis, and indophenol blue was used to evaluate NH_3 production and FE of catalysts (details of the indophenol blue method procedure are included in the ESI†). The confirmation of *i–t* measurements in 0.1 M K_2SO_4 electrolyte at −0.7 V *vs.* RHE to identify NH_3 generated by nitrate ions is shown in Fig. 4(b).

The electrochemical process of converting nitrate ions to ammonia requires eight electron transitions. We initially standardized ammonia and hydrazine so that we would know the precise concentration of ammonia and hydrazine solution, as shown in Fig. S4 and S5,† which is necessary for our final goal of ammonia manufacturing. In order to calculate the amount of nitrate converted by the $Cu_xO/Ti_3C_2T_x$ composite, half-hour-long chronoamperometric measurements were recorded at several potentials while the solution included nitrate electrolyte. Fig. 4(c) and (d) displays the results of a spectroscopic investigation, which determined that the NH_3 yield and FE at −0.7 V *vs.* RHE were approximately 41 982 μg h^{-1} m_{cat}^{-1} and 48%, respectively. We found that the NH_3 production was slightly less at −0.7 V *vs.* RHE as compared to −0.8 V *vs.* RHE, but the FE was the highest at −0.7 V *vs.* RHE; thus, we consider it as the optimized potential. Additionally, the nitrate reduction reaction comparison study of Cu_xO, $Ti_3C_2T_x$, and $Cu_xO/Ti_3C_2T_x$ composite was examined at −0.7 V against RHE. The spectroscopic examination results for the composites are displayed in Fig. S3(c) and (d).† In the case of Cu_xO, the NH_3 yield and FE at

−0.7 V *vs.* RHE were approximately 3987 μg h^{-1} m_{cat}^{-1} and 22%, respectively. The bare $Ti_3C_2T_x$ delivered NH_3 yield and FE at −0.7 V *vs.* RHE were approximately 3175 μg h^{-1} m_{cat}^{-1} and 21%, respectively. Thus, the optimized $Cu_xO/Ti_3C_2T_x$ composite delivered better NH_3 yield and the highest FE compared to Cu_xO and $Ti_3C_2T_x$. Generally, another product, hydrazine, which could be generated during nitrate reduction, was investigated. As shown in Fig. S6(c) and (e),† no UV-Vis absorption peak was found at 460 nm, and there was no colour associated with hydrazine. As a result, the selective conversion of nitrate to NH_3 is confirmed.

The stability of catalysts can be evaluated by comparing the amount of NH_3 produced to the number of cycles the catalyst has undergone. As a result, ten successive cycles of the $Cu_xO/Ti_3C_2T_x$ catalyst were performed for half an hour at −0.7 V *vs.* RHE, as shown in Fig. 5(a). The detailed spectroscopic analysis of the NH_3 production process is depicted in Fig. 5(b) and S5.† The NH_3 production drops by as much as 60% after 10 cycles as the number of cycles increases. However, after 10 cycles, the average FE dropped by only 3% from the initial FE, as shown in Fig. 5(c) and (d). As shown in Fig. S7,† no UV-Vis absorption peak was found at 460 nm after 10 cycles as there was no colour associated with hydrazine. In addition, *i–t* measurements were performed for 8 hours on the $Cu_xO/Ti_3C_2T_x$ catalyst at −0.7 V *vs.* RHE to get insight into the catalyst's stability (see Fig. S8†). After 8 hours, the current density slightly changed, demonstrating the composite's remarkable stability.

In addition, the electrochemically active surface area (ECSA) was analysed for Cu_xO, $Ti_3C_2T_x$, and $Cu_xO/Ti_3C_2T_x$ composites as shown in Fig. S9(a) and (b).† Commonly, double layer capacitance is correlated to the capacitive current and the scan rate by the following equation:[26]

$$I_{dl} = C_{dl} \times \text{scan rate}$$

where I_{dl} is the capacitive current and C_{dl} is the electrochemical double layer capacitance. Thus, C_{dl} (F cm^{-2}) can be achieved from the slope of the curve of I_{dl} plotted as a function of scan rate. Afterwards, the ECSA of various catalysts was calculated using the following equation,[27]

$$\text{ECSA} = C_{dl}/C_s$$

where C_s is the specific capacitance of catalyst material (F cm^{-2}). For the subsequently prepared transition metal-based composite, the specific capacitance value used for the

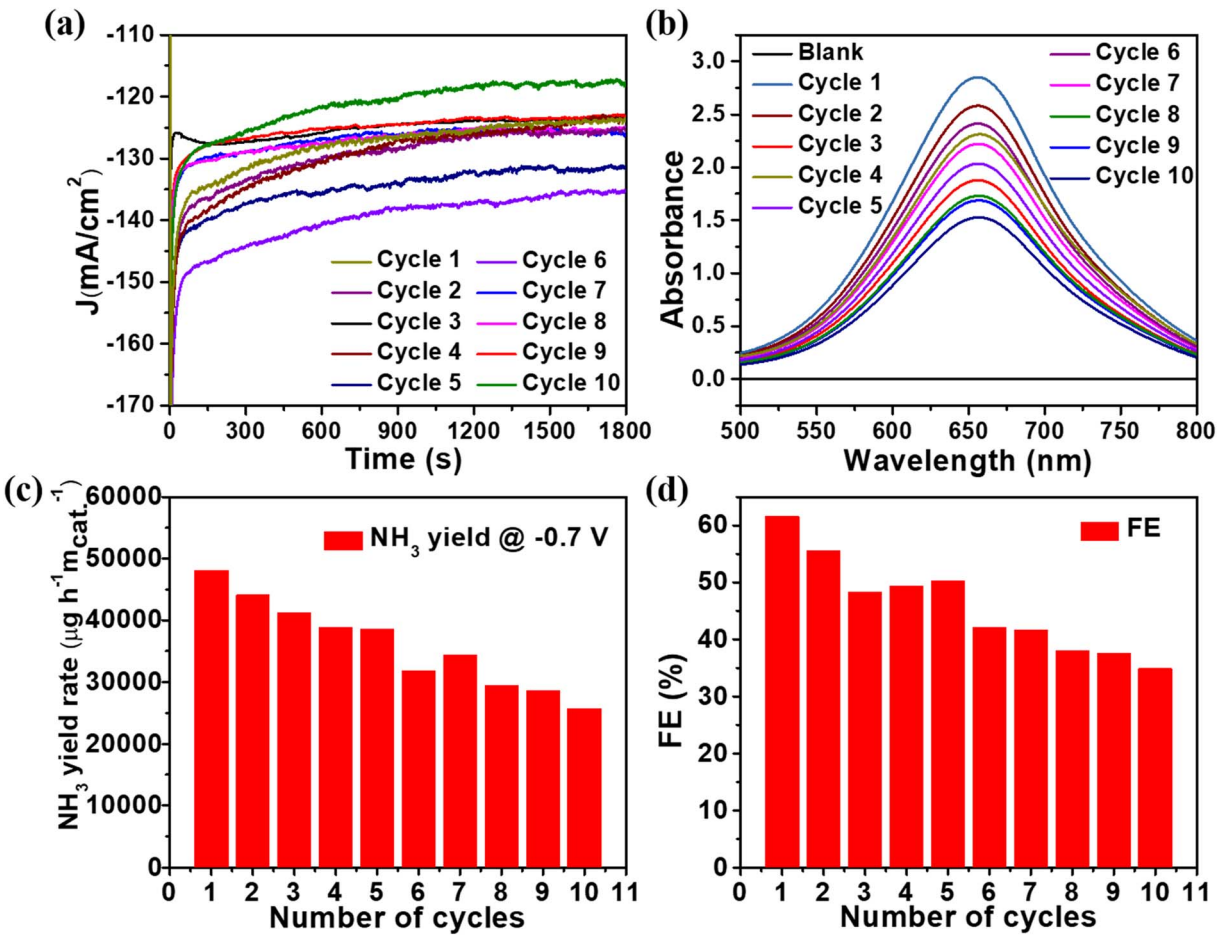

Fig. 5 (a) Chronoamperometric measurements at −0.7 V *vs.* RHE (b) UV-Vis spectra (c) NH_3 yield and (d) faradaic efficiency for NH_3 production of $Cu_xO/Ti_3C_2T_x$ catalyst.

calculation is 0.040 mF cm^{-2}. In the same way, the roughness factors (RF) of the electrodes for all electrocatalysts were determined by dividing the surface area of the electrode by the obtained ECSA value (RF = ECSA/0.0707 cm^2). In the present work, the CV analyses were carried out in the potential range from 0.1 to 0.3 V *vs.* RHE at different scan rates (20, 50, 70, and 100 mV s^{-1}). The ECSA values found from the non-faradaic region for Cu_xO, $Ti_3C_2T_x$, and $Cu_xO/Ti_3C_2T_x$ were found to be 0.0085 m^2 g^{-1}, 0.11875 m^2 g^{-1}, and 0.0114 m^2 g^{-1}, respectively (Fig. S9(a)†), while the roughness factors were obtained as 0.068, 0.945, and 0.091, respectively, as shown in Fig. S9(b).† Due to capacitive behavior, bare $Ti_3C_2T_x$ displayed higher ECSA and roughness factor than other composites, it slightly helped to enhance the active surface area and electric conductivity for the composite when compared to Cu_xO. However, because NO_3RR is associated with ammonia production, it depends on faradaic efficiency and product yield, where $Cu_xO/Ti_3C_2T_x$ produces the most relative to the other two. Thus, it is clear that the catalytic performance of $Ti_3C_2T_x$ and Cu_xO is inferior as compared to the optimized $Cu_xO/Ti_3C_2T_x$ composite. This is because $Ti_3C_2T_x$ alone (consisting of a negatively charged surface) is unfavourable for adsorbing the electron-rich nitrate due to electrostatic repulsion. Whereas, Cu_xO is favourable but the poor conductivity properties decrease the electroreduction of nitrate ions. As a result, as compared to either Cu_xO or $Cu_xO/Ti_3C_2T_x$ alone, the combination of $Ti_3C_2T_x$ and Cu_xO provides an excellent response for the nitrate reduction reaction.

5. Conclusion

In summary, we successfully constructed a $Cu_xO/Ti_3C_2T_x$ composite *via* a combustion approach for electrochemical NH_3 synthesis. The development of Cu_xO nanofoam on the $Ti_3C_2T_x$ surface improved the catalytic conversion of NO_3^- to NH_3. This is because Cu_xO is an excellent candidate for adsorbing nitrate ions and reducing it to NH_3. The improved nitrate reduction reaction with $Cu_xO/Ti_3C_2T_x$ is considerably superior as compared to Cu_xO-2/$Ti_3C_2T_x$ and Cu_xO-3/$Ti_3C_2T_x$. Electrochemical experiments of $Cu_xO/Ti_3C_2T_x$ reveal an interesting NO_3RR with a current density of 162 mA cm^{-2}. Furthermore, the $Cu_xO/Ti_3C_2T_x$ exhibits electrocatalytic activity with ammonia production of 41 982 μg h^{-1} m_{cat}^{-1} and a faradaic efficiency of 48% at −0.7 V *vs.* RHE. As a result, the performance of $Cu_xO/Ti_3C_2T_x$ indicates that it is a good candidate for nitrate ion conversion to ammonia. Furthermore, $Cu_xO/Ti_3C_2T_x$ composites may be a promising candidates in the future since they meet the parameters for an electrocatalyst for NO_3 reduction to ammonia.

Author contributions

Sagar Ingavale: conceptualization, investigation, methodology, writing – original draft, writing – review & editing. Phiralang Marbaniang: conceptualization, methodology, writing – original draft. Manoj Palabathuni: investigation, methodology. Nimai Mishra: funding acquisition, resources, supervision, writing – review & editing.

Conflicts of interest

The authors declare no conflict of interest.

Acknowledgements

We acknowledge the HRTEM facility at SRMIST set up with support from MNRE (project no. 31/03/2014-15/PVSER&D), Government of India. S. I. thanks SRM University, Andhra Pradesh, for financial support.

References

1 Y. Zhang, X. Chen, W. Wang, L. Yin and J. C. Crittenden, *Appl. Catal., B*, 2022, **310**, 121346.
2 S. Ingavale, P. Marbaniang, M. Palabathuni, V. N. Kale and N. Mishra, *Nanoscale*, 2023, 11497–11505.
3 N. C. Kani, N. H. L. Nguyen, K. Markel, R. R. Bhawnani, B. Shindel, K. Sharma, S. Kim, V. P. Dravid, V. Berry, J. A. Gauthier and M. R. Singh, *Adv. Energy Mater.*, 2023, 2204236, early view.
4 F. Jiao and B. Xu, *Adv. Mater.*, 2019, **31**, 1805173.
5 J. Wang, S. Chen, Z. Li, G. Li and X. Liu, *ChemElectroChem*, 2020, **7**, 1067–1079.
6 Y. Huang, D. D. Babu, Z. Peng and Y. Wang, *Adv. Sci.*, 2020, **7**, 1902390.
7 L. Li, C. Tang, H. Jin, K. Davey and S. Z. Qiao, *Chem*, 2021, **7**, 3232–3255.
8 H. Shen, C. Choi, J. Masa, X. Li, J. Qiu, Y. Jung and Z. Sun, *Chem*, 2021, **7**, 1708–1754.
9 J. Li, Y. Zhang, C. Liu, L. Zheng, E. Petit, K. Qi, Y. Zhang, H. Wu, W. Wang, A. Tiberj, X. Wang, M. Chhowalla, L. Lajaunie, R. Yu and D. Voiry, *Adv. Funct. Mater.*, 2022, **32**, 2108316.
10 H. Chen, Y. Pang, Y. Wei, X. He, Y. Zhang and L. Xie, *Environ. Sci. Pollut. Res.*, 2022, **114**, 1–10.
11 M. Varsha, P. S. Kumar and B. S. Rathi, *Chemosphere*, 2022, **287**, 132270.
12 T. R. Kumaraswamy, S. Javeed, M. Javaid and K. Naika, *Fresh Water Pollut. Dyn. Remediat.*, 2020, 1031, pp. 69–81.
13 F. Y. Chen, Z. Y. Wu, S. Gupta, D. J. Rivera, S. V. Lambeets, S. Pecaut, J. Y. T. Kim, P. Zhu, Y. Z. Finfrock, D. M. Meira, G. King, G. Gao, W. Xu, D. A. Cullen, H. Zhou, Y. Han, D. E. Perea, C. L. Muhich and H. Wang, *Nat. Nanotechnol.*, 2022, **17**, 759–767.
14 W. Jung and Y. J. Hwang, *Mater. Chem. Front.*, 2021, **5**, 6803–6823.
15 J. Yuan, Z. Xing, Y. Tang and C. Liu, *ACS Appl. Mater. Interfaces*, 2021, **13**, 52469–52478.
16 Q. Zhao, Z. Tang, B. Chen, C. Zhu, H. Tang and G. Meng, *Chem. Commun.*, 2022, **58**, 3613–3616.
17 Z. Gong, W. Zhong, Z. He, Q. Liu, H. Chen, D. Zhou, N. Zhang, X. Kang and Y. Chen, *Appl. Catal., B*, 2022, **305**, 121021.
18 Q. Gao, H. S. Pillai, Y. Huang, S. Liu, Q. Mu, X. Han, Z. Yan, H. Zhou, Q. He, H. Xin and H. Zhu, *Nat. Commun.*, 2022, **13**, 1–12.

19 Y. Wang, W. Zhou, R. Jia, Y. Yu and B. Zhang, *Angew. Chem., Int. Ed.*, 2020, **59**, 5350–5354.
20 K. Li, Y. Lei, J. Liao and Y. Zhang, *Inorg. Chem. Front.*, 2021, **8**, 1747–1761.
21 L. X. Li, W. J. Sun, H. Y. Zhang, J. L. Wei, S. X. Wang, J. H. He, N. J. Li, Q. F. Xu, D. Y. Chen, H. Li and J. M. Lu, *J. Mater. Chem. A*, 2021, **9**, 21771–21778.
22 L. Wang, X. Yao, S. Yuan, Y. Gao, R. Zhang, X. Yu, S. T. Tu and S. Chen, *RSC Adv.*, 2023, **13**, 6264–6273.
23 X. Su, G. Feng, L. Yu, Q. Li, H. Zhang, W. Song and G. Hu, *J. Mater. Sci.: Mater. Electron.*, 2019, **30**, 3545–3551.
24 W. Lv, L. Li, Q. Meng and X. Zhang, *J. Mater. Sci.*, 2020, **55**, 2492–2502.
25 J. Yuan, J. J. Zhang, M. P. Yang, W. J. Meng, H. Wang and J. X. Lu, *Catalysts*, 2018, **8**, 171.
26 S. Ingavale, P. Marbaniang, B. Kakade and A. Swami, *Catal. Today*, 2021, **370**, 55–65.
27 S. B. Ingavale, I. Patil, H. Parse, D. C. Sesu, P. Marbaniang, N. Ramgir, B. Kakade and A. Swami, *Int. J. Hydrogen Energy*, 2019, **44**, 24922–24933.